Affine Nonlinear Control of a Multivariate Inductive Power Transfer System With Exact Linearization

Chen Cheng, Ye Zhihao, Huang Jing, Yu Yanjuan, Xia Yihui, Gao JianXin, and Zhou Hong

***Abstract*— In this article, an exact linearization algorithm and nonlinear control scheme of the inductive power transfer (IPT) system for electric vehicles (EVs) are proposed, considering a variation in system operating point. For ease of modeling, the secondary side of IPT system is equivalent to a reflected reactor and resistor on primary side at different operating frequencies. By utilizing the exact linearization method, the nonlinear model is accurately transformed into a linear one at whole operating points. Besides, to acquire constant current\voltage (CV/CC) charging and zero voltage switching (ZVS) operating for EVs, the controllers are designed and optimized in the linear space, and then inverse mapped to the nonlinear space. This avoids designing different controllers for each operating point. Compared with a traditional PI controller, the nonlinear control scheme suggested in this article enables the system to obtain a fixed dynamic response even if the operating point of the IPT system changes. Finally, practical results obtained from a hardware prototype are included. They confirm the performances of the system and indicate that the proposed nonlinear control scheme can automatically maintain CC\CV output and ZVS operation with a constant response time of 10 ms.**

***Index Terms*—Affine nonlinear control, exact linearization, inductive power transfer (IPT), zero voltage switching (ZVS).**

I. Introduction

INDUCTIVE power transfer (IPT), which accomplishes power transfer via an alternating magnetic field without mechanical contacts is a safer, more convenient, and flexible energy delivery method compared with conventional methods. Such desirable features of IPT systems present numerous advantages like electric isolation and safe operation in harsh environments, making them suitable for a large number of applications, including electric vehicles (EVs) [1]–[4], home appliances [5], biomedical implantable devices [6], and other industrial areas [7], [8].

In these applications, the control of the IPT systems is a major research target of interest. To prevent degradation of battery life and reduce system switching loss, the IPT systems need to maintain constant current\voltage (CC\CV) charging and zero voltage switching (ZVS) operating. However, a common challenge for the control system is that the dynamic performances are sensitive to parameter perturbation and disturbances, especially when the load of the system or the set value of the control loops changes [9].

In the previous literature, most of the solutions to this problem are directly using proportional integral derivative control (PID) [1], [2], [10], Phase-locked-loop control (PLL) [6], [11], [12] and other algorithms to regulate the charging current, voltage, and ZVS angle [13], [14]. Authors in [1] and [2] have investigated a ZVS operation closed loop and two CC\CV output closed loops, which consisted of PID controllers. PLL regulation plans are introduced in [11] and [12] to adjust system operating frequency and achieve ZVS operating. However, although both the output voltage/current and ZVS angle in these papers can reach desired states with the help of the proposed control schemes, the parameters of the control loops are not optimized.

In order to tune a frequency controller through proportion-integral (PI) action, an empirical method for IPT systems is employed in [3], [15], and [16]. Besides, the neural network method is used to optimize the controller parameters [17], [18]. Since the dynamic model has not been studied in detail, the characteristics of IPT systems are neither analyzed nor considered in the controller design process, resulting in inaccurate parameters. To optimize the controller, a dynamic multivariable state-space model [19]–[21] and a two-port network model [1], [22] are proposed, respectively. However, the nonlinear effect of these models still becomes a major obstacle hindering the controller design process [23], [24]. Based on the coupled-mode theory (CMT) [25], a dynamic nonlinear model covering the phase angles and amplitudes of the coupling network is suggested [8], [26] and linearized by utilizing the small signal linearization method [27]. Similarly, in order to achieve CC/CV charging and ZVS operating for IPT systems, a lower linear fractional transformation model [9] and a small signal linear model [4], [28], [29] are proposed to optimize the dynamic performances in terms of the requirements. For example, in [4], the parameters of controllers are designed by calculating the time constant of the closed-loop dominant poles. However, a phenomenon has been observed that the dynamic performances of these traditional PI controllers that based on the simplified small signal linear model are sensitive to the changes of the system operating point caused by the load perturbations and set value modification. When the system load or set value of the control loop changes, the dynamic

Manuscript received August 30, 2019; revised March 29, 2020; accepted April 22, 2020. Date of publication April 28, 2020; date of current version July 31, 2020. This work was supported in part by the National Natural Science Foundation of China under Projects 51807197 and 61873195, and in part by the supported by the Natural Science Foundation of Hubei Province under Project 2018CFA008. Recommended for publication by Associate Editor P. Barbosa. *(Corresponding authors: Ye Zhihao; Yu Yanjuan.)*

Chen Cheng, Ye Zhihao, Huang Jing, Yu Yanjuan, Xia Yihui, and Gao JianXin are with the the School of Electrical Engineering, Naval University of Engineering, Wuhan 430032, China (e-mail: chencheng_wpt@whu.edu.cn; yxyx928@126.com; hjing99421@126.com; yuyanjuan@whu.edu.cn; xiayihui2005@163.com; gaojianxin_cn@163.com).

Zhou Hong is with the the School of Electrical Engineering and Automation, Wuhan University, Wuhan 430032, China (e-mail: hzhouwuhee@whu.edu.cn).

Color versions of one or more of the figures in this article are available online at https://ieeexplore.ieee.org.

Digital Object Identifier 10.1109/TPEL.2020.2991230

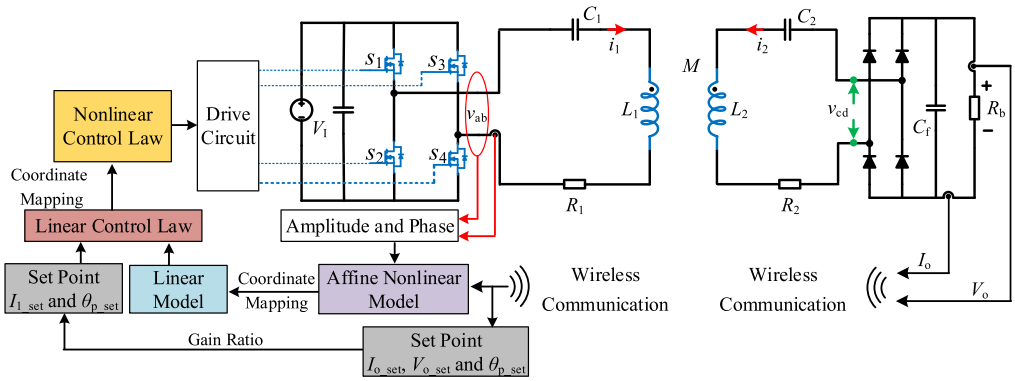

Fig. 1. Structure of the proposed IPT system.

performance of the controller will deviate its designed value. This is not friendly to those industrial applications, where the control system is required to be designed tightly in terms of the performance requirements.

In order to reduce the sensitivity of the system performance to the operating points, this article proposes an exact linearization algorithm and a nonlinear control scheme for IPT systems. In order to facilitate system modeling, the main circuit of the IPT system is simplified at different operating frequencies. Based on the equivalent circuits, a low-order nonlinear model is obtained. After the conditions for exact linearization is proved, the nonlinear model is transformed into a linear one at whole operation points. Moreover, to achieve CC/CV charging and ZVS operating, a nonlinear controller is designed and optimized in the linear space, then inverse mapped to the nonlinear space. Differentiating from the existing works, the contributions of this article are as follows.

1) Utilizing the proposed exact linearization algorithm, the dynamic nonlinear model of IPT systems can be accurately transformed into a linear one. This avoids designing different controllers for each operating point.
2) Compared with the traditional PI controller, the nonlinear control scheme adopted in this article enables the IPT system to obtain a fixed dynamic performance even if the operating point changes.

The rest of this article is organized as follows: Section II analyzes and simplifies the circuit of the system. In addition, a nonlinear control scheme is proposed. Section III focuses on the dynamic nonlinear modeling and coordinate mapping. Section IV designs the parameters of the controller, and analyzes the transmission efficiency. A simulation circuit and a hardware prototype are set up in Section V to verify the proposed nonlinear controller and its performance. Finally, Section VI concludes this article.

II. Analysis and Simplification of a Series–Series Compensated IPT System

A. System Structure

A comom series–series (S–S) compensated topology of the IPT system is shown in Fig. 1, which consists of a dc input voltage $V_{\rm I}$, a controllable Class D full-bridge inverter, two symmetrical resonant tanks, a Class D current-driven rectifier, and a load $R_{\rm b}$. Each resonant tank comprises a series capacitor C_n, inductor L_n and its equivalent series resistor (ESR) R_n $(n = 1, 2)$, respectively. $C_{\rm f}$ is the filter capacitor of the rectifier. M is the mutual inductance between two coils. The symbols i_1 and i_2 are the resonance currents through the coils; v_1 and v_2 are the voltages across the capacitors.

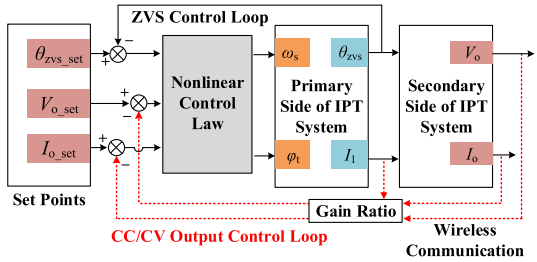

Fig. 2. Control diagram of the nonlinear control scheme.

Fig. 2 shows the control diagram of the nonlinear control scheme. To achieve CC/CV charging and ZVS operating, the operating angular frequency $\omega_{\rm s}$ and phase shift angle $\varphi_{\rm t}$ of the Class D full-bridge inverter are adjusted by a nonlinear control scheme. By detecting the charging voltage/current and ZVS angle, the IPT system can reach the set values with a fixed dynamic response speed.

B. Circuit Equivalent and Analysis

The analysis and equivalent of any circuit is necessary for developing a dynamic model, especially in the controller design process. In this section, the equivalent circuit for a S–S compensated IPT system is derived based on the following assumptions.

1) The resonant current i_1 and i_2 through the resonance network are nearly sinusoidal.
2) The filter capacitance of the full-bridge rectifier is large enough so that the ripple of the output voltage can be neglected.

Based on these assumptions, the equivalent resistance of the rectifier load can be derived as [30]

$$R_{\rm cd} = 8R_{\rm b}/\pi^2. \tag{1}$$

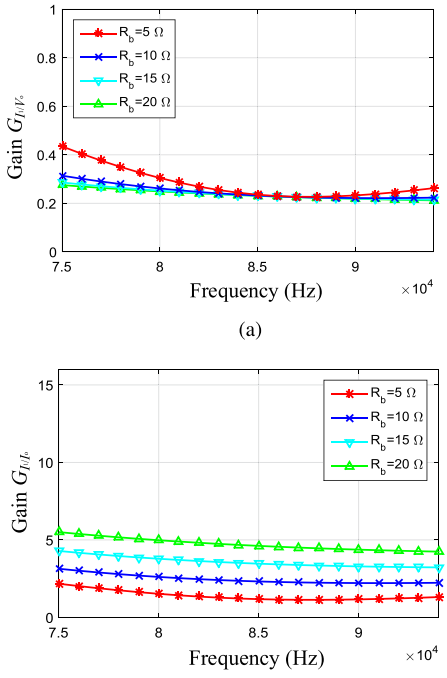

Fig. 3. Normalized gains $G_{I_{1\mathrm{rms}}/I_\mathrm{o}}$ and $G_{I_{1\mathrm{rms}}/V_o}$ versus ω_s for various values of R_b. (a) $G_{I_{1\mathrm{rms}}/I_\mathrm{o}}$ as functions of ω_s. (b) $G_{I_{1\mathrm{rms}}/V_o}$ as functions of ω_s.

For Class D full-bridge inverter, the phase shift angle φ_t of the pulsewidth modulated (PWM) signal can be regulated form 0^o to 180^o. Accordingly, the output voltage of the inverter can be changed by the adjustment of φ_t as follows:

$$v_\mathrm{ab} = \frac{4}{\pi}\cos\frac{\varphi_\mathrm{t}}{2}V_\mathrm{I}\sin\left(\omega_\mathrm{s}t\right). \tag{2}$$

Thus, the resonant currents i_1 and i_2 are

$$\begin{cases} i_1 = v_\mathrm{ab}/\left(Z_1 + Z_{2\mathrm{reflect}}\right) \\ i_2 = j\omega_\mathrm{s}Mi_1/Z_2 \end{cases} \tag{3}$$

where Z_1 and Z_2 are the primary and secondary side impedance, respectively. $Z_{2\mathrm{reflect}}$ is the secondary side impedance reflected to the primary side. From (3), the gains of $I_{1\mathrm{rms}}/I_\mathrm{o}$ and $I_{1\mathrm{rms}}/V_\mathrm{o}$ for different ω_s can be found as

$$\begin{cases} G_{I_{1\mathrm{rms}}/I_\mathrm{o}} = \frac{I_{1\mathrm{rms}}}{I_\mathrm{o}} = \frac{\pi}{2\sqrt{2}}\frac{(Z_2+R_\mathrm{cd})}{j\omega_\mathrm{s}M} \\ G_{I_{1\mathrm{rms}}/V_\mathrm{o}} = \frac{I_{1\mathrm{rms}}}{V_\mathrm{o}} = \frac{2\sqrt{2}}{\pi}\frac{Z_2+R_\mathrm{cd}}{j\omega_\mathrm{s}MR_\mathrm{cd}} \end{cases} \tag{4}$$

where $I_{1\mathrm{rms}}$ is the rms value of i_1. Plots of $G_{I_{1\mathrm{rms}}/I_\mathrm{o}}$ and $G_{I_{1\mathrm{rms}}/V_\mathrm{o}}$ against ω_s for various values of R_b are depicted in Fig. 3(a) and (b). Assuming that the system parameters and load resistance are constant, the gain curves $G_{I_{1\mathrm{rms}}/I_\mathrm{o}}$ and $G_{I_{1\mathrm{rms}}/V_\mathrm{o}}$ are only related to the operating angular frequency ω_s. In other words, the system output current and voltage can be controlled by adjusting the primary current i_1 [10], [31].

The reflected impedance $Z_{2\mathrm{reflect}}$ can be expressed as

$$Z_{2\mathrm{reflect}} = \frac{1}{eq_1}\left(\left(\omega_\mathrm{s}C_2\right)\left(R_2+R_\mathrm{cd}\right) + j\left(1-\omega_\mathrm{s}^2L_2C_2\right)\right) \tag{5}$$

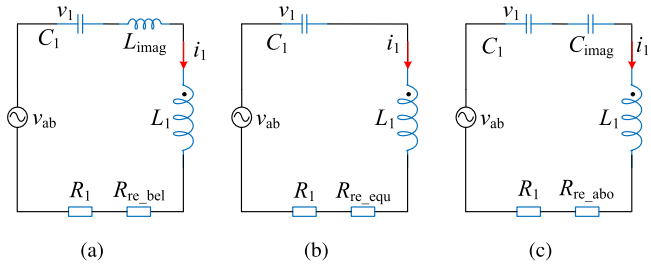

Fig. 4. Primary side equivalent circuit for different operating angular frequency ω_s. (a) for $\omega_\mathrm{s} < \omega_2$. (b) for $\omega_\mathrm{s} = \omega_2$. (c) for $\omega_\mathrm{s} > \omega_2$.

where

$$eq_1 = \frac{\left(\omega_\mathrm{s}M\right)^2\left(\omega_\mathrm{s}C_2\right)}{\left(R_2+R_\mathrm{cd}\right)^2\left(\omega_\mathrm{s}C_2\right)^2 + \left(\omega_\mathrm{s}^2L_2C_2-1\right)^2}. \tag{6}$$

Observation of (5) indicates that the reflected impedance $Z_{2\mathrm{reflect}}$ consists of real part and imaginary part, which are determined by ω_s. Thus, (5) can be rewritten as follows:

$$Z_{2\mathrm{reflect}} = \begin{cases} R_{\mathrm{re\_bel}} + j\omega_\mathrm{s}L_\mathrm{imag}, & \omega_\mathrm{s} < \omega_2 \\ R_{\mathrm{re\_equ}}, & \omega_\mathrm{s} = \omega_2 \\ R_{\mathrm{re\_abo}} + 1/\left(j\omega_\mathrm{s}C_\mathrm{imag}\right), & \omega_\mathrm{s} > \omega_2 \end{cases} \tag{7}$$

where ω_2 is the resonant angular frequency of the secondary side. Thus, the secondary side of the IPT system can be equivalent to a reflected reactor and a reflected resistor on the primary side circuit for different ω_s as shown in Fig. 4.

In this article, the startup operating frequency is designed to be slightly lower than the resonant frequency of secondary side to achieve an inductive reflection impedance. In addition, the proposed nonlinear control scheme can ensure that the system always obtains ZVS operation by adjusting the operating frequency. Thus, the following sections will take Fig. 4(a) as an example to introduce the exact linearization algorithm and nonlinear control scheme.

III. Modeling, Exact Linearization, and Nonlinear Control of the System

A. Dynamic Model of a Primary-Side Equivalent Circuit

Referring to Fig. 4(a), the dynamic behaviors of the IPT system can be described by the following second-order differential equations:

$$\begin{cases} \frac{di_1}{dt} = \frac{1}{L_1+L_\mathrm{imag}}\left(v_\mathrm{ab} - i_1\left(R_1+R_{\mathrm{re\_bel}}\right) - v_1\right) \\ \frac{dv_1}{dt} = \frac{1}{C_1}i_1 \end{cases} \tag{8}$$

where L_imag and $R_{\mathrm{re\_bel}}$ are, respectively the reflected resistance and inductance obtained from (7). Besides, in order to realize ZVS operating control, the description of the ZVS angle also needs to be included in the equations. Therefore, according to the CMT [25], the state variables i_1 and v_1 are represented by the mode amplitude a_1 and mode phase angle θ_1 of the primary side as [8], [27]

$$\begin{cases} i_1 = \sqrt{\frac{2}{L_1+L_\mathrm{ima}}}\cdot a_1\cos\left(\omega_\mathrm{s}t+\theta_1\right) \\ v_1 = \sqrt{\frac{2}{C_1}}\cdot a_1\sin\left(\omega_\mathrm{s}t+\theta_1\right). \end{cases} \tag{9}$$

This together with (8), a dynamic nonlinear state-space model, which can describe the primary side current and phase angle is given in

$$\begin{cases} \frac{dx_1}{dt} = \frac{1}{\sqrt{2(L_1+L_{\text{imag}})}}\left(\frac{V_I}{\pi}u_1\cos(x_2) - \frac{x_1(R_1+R_{\text{re\_bel}})}{\sqrt{2(L_1+L_{\text{imag}})}}\right) \\ \frac{dx_2}{dt} \\ \quad = -u_2 + \frac{1}{\sqrt{(L_1+L_{\text{imag}})C_1}} - \frac{1}{x_1\sqrt{2(L_1+L_{\text{imag}})}}\frac{2V_I}{\pi}u_1\sin(x_2) \end{cases} \tag{10}$$

where $x = [x_1,\ x_2]^{\mathrm{T}} = [a_1,\ \theta_1]^{\mathrm{T}}$ is the state vector, and $u = [u_1, u_2]^{\mathrm{T}} = [\cos(\varphi_{\mathrm{t}}/2), \omega_{\mathrm{s}}]^{\mathrm{T}}$ is the control vector. In order to adjust the primary current i_1, and then get controllable outputs, the following output functions are defined as:

$$\begin{cases} h_1(x) = \sqrt{\frac{2}{L_1+L_{\text{imag}}}}x_1 - I_{1\text{set}} \\ h_2(x) = x_2 - \theta_{\text{zvsset}} \end{cases} \tag{11}$$

where $I_{1\text{set}}$ and θ_{zvsset}, respectively are the set values of I_1 and ZVS angle θ_{zvs}. It can be observed from (10) that the IPT system is linear with respect to u vector. Therefore, combined with $h_1(x)$ and $h_2(x)$, the model (10) can be written in the form of an affine nonlinear model as follows:

$$\begin{cases} \dot{x} = f(x) + g_1(x)u_1 + g_2(x)u_2 \\ y_1 = h_1(x) \\ y_2 = h_2(x). \end{cases} \tag{12}$$

The symbols $f(x)$ and $g(x)$ are the smooth vector fields, namely

$$\begin{cases} f(x) = \begin{pmatrix} -\frac{R_1+R_{\text{re\_bel}}}{2(L_1+L_{\text{imag}})}x_1 \\ \frac{1}{\sqrt{(L_1+L_{\text{imag}})C_1}} \end{pmatrix} \\ g_1(x) = \begin{pmatrix} \alpha\cos(x_2) \\ -2\alpha\sin(x_2)/x_1 \end{pmatrix} \\ g_2(x) = \begin{pmatrix} 0 \\ -1 \end{pmatrix} \end{cases} \tag{13}$$

where

$$\alpha = \frac{V_{\mathrm{I}}}{\left(\pi\sqrt{2\left(L_1 + L_{\text{imag}}\right)}\right)}. \tag{14}$$

B. Analysis of Exact Linearization Conditions

In this section, the exact linearization conditions for the proposed IPT system are analyzed and verified based on the feedback linearization theory.

Theorem 1: Consider a multivariate affine nonlinear system with n variables, suppose that the number of the inputs is equal to the order of the system. The system can be exact linearized into a Brunovsky-standard linear system if, and only if, there exists a function $\gamma(x)$ such that the following conditions hold:

1) The matrices of the vector fields

$$\boldsymbol{D}_n = [g_1(x)\ g_2(x)\ ...\ g_n(x)] \tag{15}$$

are linearly independent at all operating points.

2) The set

$$\begin{cases} \boldsymbol{D}_1 = [g_1(x)] \\ \boldsymbol{D}_2 = [g_1(x)\ g_2(x)] \\ \vdots \\ \boldsymbol{D}_n = [g_1(x)g_2(x)\cdots g_n(x)] \end{cases} \tag{16}$$

is involutive.

This controllability condition and the involutivity condition are proved in [32]. For a IPT system in this article, the matrixes of the vector fields can be written as follows:

$$\boldsymbol{D}_1 = [g_1(x)]|_{x_1\neq 0} = \begin{bmatrix} \alpha\cos(x_2) \\ -2\alpha\sin(x_2)/x_1 \end{bmatrix} \tag{17}$$

$$\boldsymbol{D}_2 = [g_1(x)\ g_2(x)]|_{x_1\neq 0} = \begin{bmatrix} \alpha\cos(x_2) & 0 \\ -2\alpha\sin(x_2)/x_1 & -1 \end{bmatrix}. \tag{18}$$

Equations (17) and (18) indicate that the ranks of $\boldsymbol{D}_1$ and $\boldsymbol{D}_2$ are equal to their dimensions. In other words, the matrices of vector fields for the system are linearly independent. In addition, the Lie bracket of $g_1(x)$ to $g_2(x)$ is

$$\mathrm{ad}_{g_1(x)}g_2(x) = -\begin{bmatrix} -\alpha\sin(x_2) \\ 2\alpha\left(\sin(x_2)/x_1 - \cos(x_2)\right)/x_1 \end{bmatrix}. \tag{19}$$

Combining (17)–(19) yields the augmented matrix as

$$\begin{aligned} &\left[g_1(x)\ \ g_2(x)\ \ \mathrm{ad}_{g_1(x)}g_2(x)\right] \\ &= \begin{bmatrix} \alpha\cos(x_2) & 0 & -\alpha\sin(x_2) \\ -\frac{2\alpha\sin(x_2)}{x_1} & -1 & \frac{2\alpha}{x_1}\left(\frac{\sin(x_2)}{x_1} - \cos(x_2)\right) \end{bmatrix}. \end{aligned} \tag{20}$$

This also shows that the rank of the augmented matrix is equal to its dimension. According to the $FrobeniusTheorem$ [32], the set of $g_1(x)$ and $[g_1(x), g_2(x)]$ is said to be involutive. Therefore, the conditions of the exact linearization for IPT system at $\omega_{\mathrm{s}} < \omega_2$ are satisfied. By observing (17)–(20), it should be noted that the controllability condition and the involutivity condition are independent of ω_{s}. This implies that the modeling and exact linearization methods studied in this article are also applicable to a resistive or capacitive impedance reflected in Fig. 4.

C. Exact Linearization Algorithm of the IPT System

Fig. 5 depicts the diagram of the coordinate mapping algorithm. First, a set of linear independent vector fields in terms of (17) and (18) are selected to describe the IPT system in the nonlinear x space. Second, based on the principle of the intergralcurve [33], the coordinate mapping $x = \boldsymbol{F}(\gamma)$, which is from the γ space to the x space is deduced by solving the differential equations. Then, according to the coordinate inverse mapping, the mapping relationship $\boldsymbol{R}_{n-1}$, which is from the γ space to the linear z space are defined. Therefore, the final composite mapping T, which is from x space to a linear z space is obtained by combining $\boldsymbol{F}^{-1}$ and $\boldsymbol{R}_{n-1}$. Moreover, using the composite mapping T, the vector fields of the affine nonlinear model $f(x)$, $g_1(x)$, and $g_1(x)$ can be exact linearized into a Brunovsky-standard linear model.

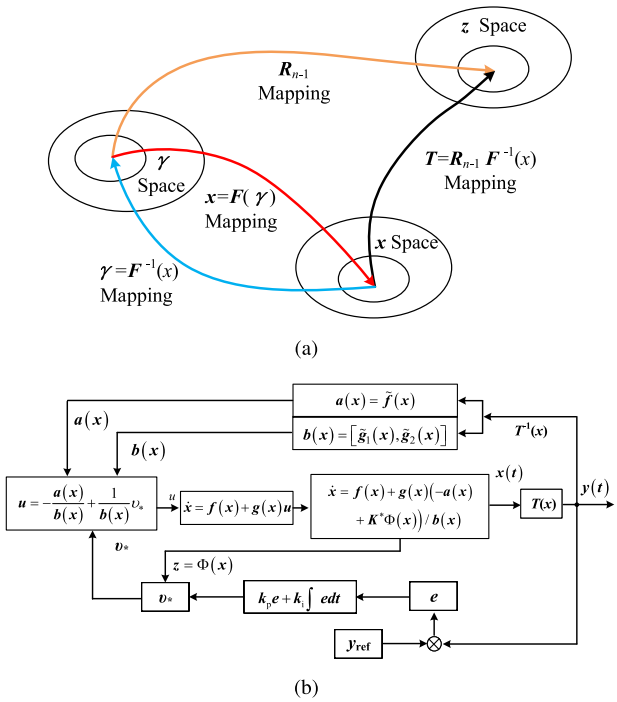

Fig. 5. Diagram of the coordinate mapping algorithm. (a) Mapping relations in space. (b) Flowchart for the exact linearization algorithm.

From (17) and (18), two simple linear independent vector fields $\bar{\boldsymbol{D}}_1 \in \boldsymbol{D}_1$ and $\bar{\boldsymbol{D}}_2 \in \boldsymbol{D}_2$ are selected as

$$\begin{cases} \bar{\boldsymbol{D}}_1 = \begin{bmatrix} -x_1 \\ 2\tan x_2 \end{bmatrix} \\ \bar{\boldsymbol{D}}_2 = \begin{bmatrix} 0 \\ 1 \end{bmatrix} \end{cases} \tag{21}$$

to satisfied

$$\begin{cases} \bar{\boldsymbol{D}}_1 + k_1^{(1)}(x) g_1(x) = 0 \\ \bar{\boldsymbol{D}}_2 + k_1^{(2)}(x) g_1(x) + k_2^{(2)} g_2(x) = 0 \end{cases} \tag{22}$$

where $k_1^{(1)} = -x_1/\alpha\cos(x_2)$, $k_1^{(2)}(x) = 0$ and $k_2^{(2)}(x) = 1$.

Based on the principle of the intergralcurve [33], the coordinate mapping $x = \boldsymbol{F}(\gamma)$ can be expressed as

$$\boldsymbol{F}(\gamma_1, \gamma_2) = \boldsymbol{\Phi}_{\gamma_1}^{\bar{\boldsymbol{D}}_1} \circ \boldsymbol{\Phi}_{\gamma_2}^{\bar{\boldsymbol{D}}_2}(x^0) \tag{23}$$

where x^0 is the initial operating point of the IPT system. The left term of (23) denotes the intergral curve of $\bar{\boldsymbol{D}}_1$ and $\bar{\boldsymbol{D}}_2$, which can be obtained by solving the following differential equations one by one. For the intergralcurve $\boldsymbol{\Phi}_{\gamma_2}^{\bar{\boldsymbol{D}}_2}(x^0)$, the differential equation is

$$\frac{d}{d\gamma_2}\begin{bmatrix} x_1 \\ x_2 \end{bmatrix} = \bar{\boldsymbol{D}}_2 = \begin{bmatrix} 0 \\ 1 \end{bmatrix}. \tag{24}$$

According to (9), the initial set value of (24) is

$$x^0 = \begin{bmatrix} x_1^0 \\ x_2^0 \end{bmatrix} = \begin{bmatrix} I_{1\text{set}}\sqrt{\frac{L_1+L_{\text{imag}}}{2}} \\ \frac{\theta_{\text{zvsset}}\pi}{180} \end{bmatrix}. \tag{25}$$

This yields the solution

$$\begin{bmatrix} x_1 \\ x_2 \end{bmatrix} = \begin{bmatrix} x_1^0 \\ \gamma_2 + x_2^0 \end{bmatrix}. \tag{26}$$

Similarly, the intergralcurve $\boldsymbol{\Phi}_{\gamma_1}^{\bar{\boldsymbol{D}}_1} \circ \boldsymbol{\Phi}_{\gamma_2}^{\bar{\boldsymbol{D}}_2}(x^0)$ is obtained by solving the differential equation

$$\frac{d}{d\gamma_1}\begin{bmatrix} x_1 \\ x_2 \end{bmatrix} = \bar{\boldsymbol{D}}_1 = \begin{bmatrix} -x_1 \\ 2\tan x_2 \end{bmatrix} \tag{27}$$

with the initial set value $x^0 = [x_1^0, \gamma_2 + x_2^0]^{\mathrm{T}}$. Therefore, one obtains the coordinate mapping $x = \boldsymbol{F}(\gamma)$, that is

$$\boldsymbol{F}(\gamma_1, \gamma_2) = \begin{bmatrix} x_1^0 e^{-\gamma_1} \\ \arcsin\left(\sin\left(\gamma_2 + x_2^0\right) e^{2\gamma_1}\right) \end{bmatrix}. \tag{28}$$

Correspondingly, the inverse coordinate mapping of $\boldsymbol{F}(\gamma_1, \gamma_2)$, namely, the mapping relationship from x space to γ space can be calculated as

$$\boldsymbol{F}^{-1}(x_1, x_2) = \begin{bmatrix} -\mathrm{In}\left(\frac{x_1}{x_1^0}\right) \\ \arcsin\left(\frac{(x_1)^2\sin(x_2)}{(x_1^0)^2}\right) - x_2^0 \end{bmatrix}. \tag{29}$$

In general, according to the export mapping of $\boldsymbol{F}^{-1}(x_1, x_2)$, one can obtain the definition of the mapping that from γ space to a linear z space. In this article, however, due to the number of the inputs is equal to the order of the system, the export mapping does not exist. Thus, the mapping relationship $\boldsymbol{R}_{n-1}$ is given by

$$\begin{cases} z_1^0 = \gamma_1 \\ z_2^0 = \gamma_2 \end{cases} \tag{30}$$

From Fig. 5, the composite mapping $\boldsymbol{T}$ can be expressed as

$$\boldsymbol{T} = \boldsymbol{R}_{\mathrm{n}-1}\boldsymbol{F}^{-1} = \begin{bmatrix} -\mathrm{In}\left(\frac{x_1}{x_1^0}\right) \\ \arcsin\left(\frac{(x_1)^2\sin(x_2)}{(x_1^0)^2}\right) - x_2^0 \end{bmatrix}. \tag{31}$$

Correspondingly, the inverse mapping $\boldsymbol{T}^{-1}$ is

$$\boldsymbol{T}^{-1}(z) = \begin{bmatrix} x_1^0 e^{-z_1} \\ \arcsin\left(\sin\left(z_2 + x_2^0\right) e^{2z_1}\right) \end{bmatrix}. \tag{32}$$

Based on the Jacobian matrix of the coordinate mapping $\boldsymbol{T}$, the vector fields of the original affine nonlinear IPT system $f(x)$, $g_1(x)$, and $g_2(x)$ can be transformed into linear vector fields of $\tilde{f}(x)$, $\tilde{g}_1(x)$ and $\tilde{g}_2(x)$. From (31), one obtains the Jacobian matrix

$$\boldsymbol{J}_T = \begin{bmatrix} \frac{\partial\gamma_1}{\partial x_1} & \frac{\partial\gamma_1}{\partial x_2} \\ \frac{\partial\gamma_2}{\partial x_1} & \frac{\partial\gamma_2}{\partial x_2} \end{bmatrix} = \begin{bmatrix} -\frac{1}{x_1} & 0 \\ \beta 2\sin(x_2) & -\beta\cos(x_2) \end{bmatrix} \tag{33}$$

where

$$\beta = \frac{x_1}{(x_1^0)^2\sqrt{1 - \left(\frac{(x_1)^2\sin(x_2)}{(x_1^0)^2}\right)^2}}. \tag{34}$$

Hence, the vector fields $\tilde{f}(x)$, $\tilde{g}_1(x)$, and $\tilde{g}_2(x)$ can be calculated as

$$\begin{cases} \tilde{f}(x) = J_T f(x) \\ = \begin{bmatrix} \frac{R_1+R_{\text{re\_bel}}}{2(L_1+L_{\text{imag}})} \\ \beta\left(-\frac{(R_1+R_{\text{re\_bel}})x_1\sin(x_2)}{L_1+L_{\text{imag}}} - \frac{\cos(x_2)}{\sqrt{(L_1+L_{\text{imag}})C_1}}\right) \end{bmatrix} \\ \tilde{g}_1(x) = J_T g_1(x) = \begin{bmatrix} -\frac{\alpha}{x_1}\cos(x_2) \\ 0 \end{bmatrix} \\ \tilde{g}_2(x) = J_T g_2(x) = \begin{bmatrix} 0 \\ \beta\cos(x_2) \end{bmatrix}. \end{cases} \tag{35}$$

Let $a(x) = \tilde{f}(x), b(x) = [\tilde{g}_1(x), \tilde{g}_2(x)]$, the nonlinear control law can be defined as

$$u = -\frac{1}{b(x)}a(x) + \frac{1}{b(x)}\upsilon_* \tag{36}$$

where υ_* is the controller of the system in linear z space. Combining (35) and (36), one arrives the final nonlinear controller in Eq. (37) as shown at the bottom of this page.

It should be noted that the nonlinear control law obtained above can be directly applied to the affine nonlinear IPT system. In addition, utilizing the inverse coordinate mapping $\boldsymbol{T}^{-1}$, the original affine nonlinear IPT system can be written in the Brunovsky normalized linear form as

$$\dot{z} = A_z z + B_z \upsilon_* \tag{38}$$

where

$$A_z = \begin{bmatrix} 0 & \\ & 0 \end{bmatrix}, B_z = \begin{bmatrix} 1 & \\ & 1 \end{bmatrix}. \tag{39}$$

This shows that the exact linearization of the nonlinear IPT system at $\omega_s < \omega_2$ has been achieved.

IV. Controller Design and Efficiency Analysis

A. Design of the Nonlinear Controller

Based on the main parameters in Table I, a transfer function matrix of the linear model at the initial operation point can be achieved as

$$G_z = \begin{bmatrix} \frac{3.2e4}{s+2.85e4} & \\ & \frac{2587}{s+1.81e4} \end{bmatrix}. \tag{40}$$

The unity feedback root locus of the transfer function matrix at different gains is plotted in Fig. 6. By analyzing the closed-loop zero-pole distribution, the following conclusion can be obtained.

1) As the gain changes, the poles of the transfer functions gradually move to the right side of the s-plane.
2) The stabilities of both output current loop and ZVS angle loop are available because the closed-loop poles are all located in the left s-plane.

TABLE I
Main Parameters of the Proposed IPT System

Symbol	Explanation	Value
L_1	Parimary side resonant inductance	33.1 μH
L_2	Secondary side resonant inductance	34.3 μH
C_1	Parimary side resonant capacitance	104.2 nF
C_2	Secondary side resonant capacitance	98.5 nF
R_1	ESR of the primary L-C network	0.04 Ω
R_2	ESR of the secondary L-C network	0.04 Ω
M	Mutual inductance	7.33 μH
V_I	DC input voltage	350 V
r_{MOS}	On resistance of the full bridge inverter	0.04 Ω
V_{D}	Forward voltage of the rectifier diodes	0.7 V
r_{cf}	Parasitic resistance of the filter capacitor	0.005 Ω
R_{D}	ESR of the diodes filter capacitor	0.005 Ω
t_{r}	Raising time of the MOSFET	28 ns
t_{f}	Falling time of the MOSFET	8 ns
$k_{\text{p1}}, k_{\text{p2}}$	Proportional coefficients	0.02,0.03
$k_{\text{i1}}, k_{\text{i2}}$	Integral coefficients	9,15
φ_{t}	Range of the phase shift angle	0-180 $^{\text{o}}$
f_s	Range of the operating frequency	75-86.5 kHz

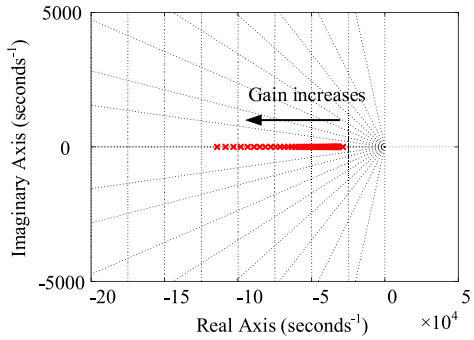

(a)

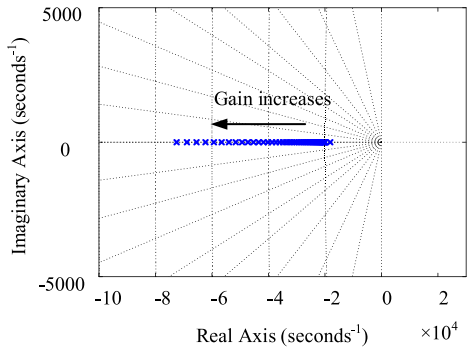

(b)

Fig. 6. Unity feedback root locus of the transfer function matrix for different gains. (a) Output current loop. (b) ZVS angle loop.

$$u = \begin{bmatrix} u_1 \\ u_2 \end{bmatrix} = \begin{bmatrix} -\frac{x_1}{\alpha\cos x_2}\left(\frac{R_1+R_{\text{re\_bel}}}{2(L_1+L_{\text{imag}})} + \upsilon_{1*}\right) \\ \frac{1}{\beta\cos x_2}\left(\beta\left(-\frac{(R_1+R_{\text{re\_bel}})x_1\sin(x_2)}{L_1+L_{\text{imag}}} - \frac{\cos(x_2)}{\sqrt{(L_1+L_{\text{imag}})C_1}}\right) + \upsilon_{2*}\right) \end{bmatrix} \tag{37}$$

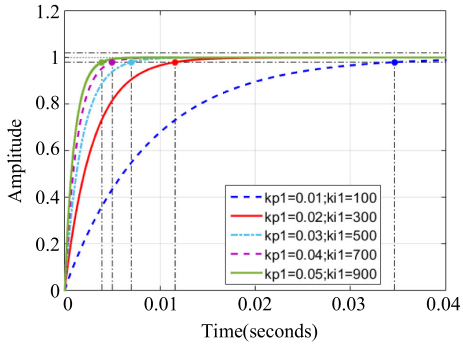

(a)

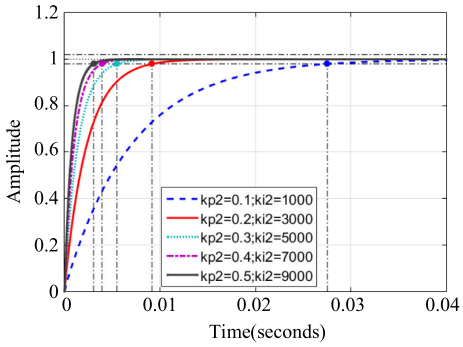

(b)

Fig. 7. Unit step response performance of the closed-loop transfer function matrix for different proportion and integration coefficients. (a) Output current loop. (b) ZVS angle loop.

In this article, a linear controller υ_* is designed to enable the output current $I_{\rm o}$, output voltage $V_{\rm o}$, and ZVS angle $\theta_{\rm set}$ of the IPT system to track their set values. Thus, according to the principle of the proportional integral control method, the linear controller υ can be defined as

$$\upsilon_* = \begin{bmatrix} k_{\rm p1}+k_{\rm i1}/s \\ k_{\rm p1}+k_{\rm i2}/s \end{bmatrix} \tag{41}$$

where $k_{{\rm p}i}$ and $k_{{\rm i}i}(i=1$ is for output current loop, $i=2$ is for ZVS angle loop) are the proportion and integration coefficient.

Substituting (41) in to (40), one obtains the closed-loop transfer function matrix consisting of υ_* as

$$\Phi_z(s) = \begin{bmatrix} \frac{2\xi_1\omega_{\rm n1}s+\omega_{\rm n1}^2}{s^2+2\xi_1\omega_{\rm n1}s+\omega_{\rm n1}^2} & \\ & \frac{2\xi_2\omega_{\rm n2}s+\omega_{\rm n2}^2}{s^2+2\xi_2\omega_{\rm n2}s+\omega_{\rm n2}^2} \end{bmatrix} \tag{42}$$

where the damping coefficients of the function matrix are

$$\begin{cases} \xi_1 = \frac{2.85e4+3.2e4K_{\rm p1}}{2\sqrt{3.2e4K_{\rm i2}}},\ \omega_{\rm n1} = \sqrt{3.2e4K_{\rm i1}} \\ \xi_2 = \frac{1.81e4+2587K_{\rm p1}}{2\sqrt{2587K_{\rm i2}}},\ \omega_{\rm n2} = \sqrt{2587K_{\rm i2}}. \end{cases} \tag{43}$$

It can be seen from (42) that the proportion and integration elements of * are equivalent to add a new closed-loop zero and a new dominant pole to each control-loop. Fig. 7 depicts the unit step response performance of the closed-loop transfer function matrix. One can see that as the proportion and integration coefficient increases, the response time of the curves gradually decreases, which indicates that dynamic performance of the controller can be further improved.

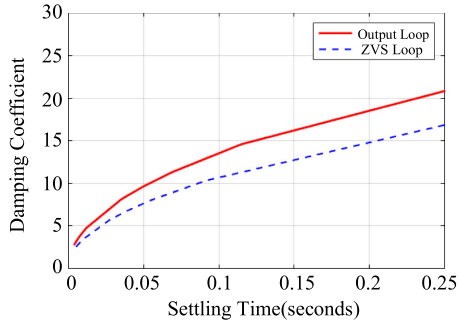

Fig. 8. Relationship between the settling times and the damping coefficients.

By analyzing the performance of the unit step response curves, the relationship between the settling times and the damping coefficients are plotted in Fig. 8. It can be seen that the settling time is directly proportional to the damping coefficient. Thus, the parameters of υ_* can be optimized by calculating the damping coefficient ξ_1 and ξ_2 according to the performance requirements.

In this article, because the obtained nonlinear control law is computationally complex, the full-bridge inverter is implemented with four MOSFET switches (IPW65R041CFD), and triggered by two micro control unit (MCU) controllers, namely, an advanced reduced instruction set computer machines (ARM) (STM32F407VGT), and an field programmable gate array (FPGA) (XC6SLX9-3TQG144I). Besides, the wireless communication link is set up with two nRF24L01 modules. Therefore, considering that the MCUs and wireless communication modules of the experimental prototype need time to compute and transmit data [28], the requirements of the settling time for each control loop are selected as 10 ms. It should be noted that the dynamic speed of 10 ms is based on our laboratory prototype, and the parameters of the controllers are designed as fast as possible. Using MATLAB, the final parameters of the proportion and integration coefficient are calculated as:$k_{\rm p1}= 0.02, k_{\rm i1}= 281$, $k_{\rm p2}= 0.2,$ and $k_{\rm i2}= 3010$.

B. *Efficiency Analysis of the System*

The transmission efficiency of the system can be calculated by where $P_{\rm load}$ is the power obtained from the load that can be achieved by measuring the current flowing through the load [34]. $P_{\rm loss} = P_{\rm Ploss} + P_{\rm Sloss}$ is the overall loss of the both sides. The power loss of the primary side $P_{\rm Ploss}$ consists of the conduction loss $P_{\rm Pconduct}$ and the inverter switching loss $P_{\rm inv}$. The primary side conduction loss is

$$P_{\rm Pconduct} = \frac{I_1^2\left(R_1+2r_{\rm MOS}\right)}{2}. \tag{44}$$

The most dominant loss present in the system is switching losses, which is generally more than conduction losses. In this article, the proposed nonlinear controller can automatically maintain ZVS operation. Therefore, the turn-ON switching loss can be ignored and only turn-OFF switching loss is calculated

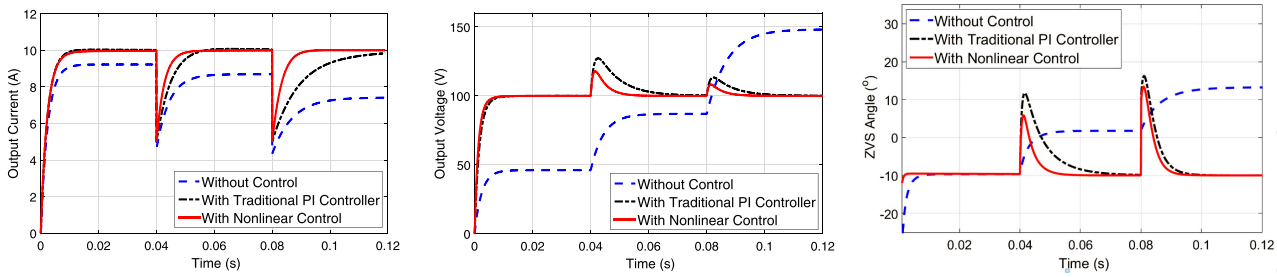

Fig. 9. Dynamic response curves of a controlled and uncontrolled IPT system for a step charging load. $R_{\rm b}$ changes from 5 to 10 Ω at $t = 0.04$ s. $R_{\rm b}$ changes from 10 to 20 Ω at $t = 0.08$ s. (a) Response curve for $I_{\rm o}$. (b) Response curve for $V_{\rm o}$. (c) Response curve for $\theta_{\rm zvs}$.

per

$$P_{\rm inv} = 4 f_{\rm s} V_{\rm I} i_1 \left(\frac{t_{\rm r}}{3} + \frac{t_{\rm f}}{2} \right) \tag{45}$$

where $t_{\rm r}$ and $t_{\rm f}$ are the rising and falling time of the MOSFET, respectively, [28], [30], [35].

For the secondary side, the overall power loss $P_{\rm Sloss}$ consists of the secondary side conduction loss $P_{\rm Sconduct}$ and rectifier power loss $P_{\rm rec}$.The secondary side conduction loss is

$$P_{\rm Sconduct} = \frac{I_2^2 R_2}{2}. \tag{46}$$

The rectifier power loss can be calculated by

$$P_{\rm rec} = 2\sqrt{2} V_{\rm D} I_2 + \frac{(2R_{\rm D} + r_{\rm cf}) I_2^2}{2} \left(\frac{\pi^2}{8} - 1 \right) \tag{47}$$

where $V_{\rm D}$ is the forward voltage of the rectifier diodes, $R_{\rm D}$ is the ESR of the rectifier diodes, and $r_{\rm cf}$ is the parasitic resistance of the rectifier filter capacitor.

V. Simulation and Experimental Verification

A. Effectiveness Simulation

In this section, the dynamic response curves of the IPT system with and without control are investigated by the means of MATLAB/Simulink toolbox. To verify the effectiveness and superiority of the control performance, the proposed nonlinear controller is compared with the traditional PI controller. Referring to the charging curve of a battery load in [4], [28], [29], and [35], the set values of the output current $I_{\rm o}$ and output voltage $V_{\rm o}$ are selected as 10 A and 100 V, respectively. In order to reduce the total power loss of the system [1], [4], it is necessary to ensure the drain–source junction capacitor parallel to the MOSFET has sufficient time to charge and discharge [30]. Therefore, the set value of the ZVS angle is selected as -10° [4], [28]. Last, based on the main parameters of the circuit, the corresponding dynamic response curves are plotted in Fig. 9 by changing the load from 5 to 10 Ω and from 10 to 20 Ω.

One can see that the output $I_{\rm o}$, $V_{\rm o}$, and $\theta_{\rm zvs}$ are steady-state stable regardless of the usage of controllers. However, without controller, the output $I_{\rm o}$, $V_{\rm o}$, and $\theta_{\rm zvs}$ (dashed line in Fig. 9) can not achieve the desired output value when the load resistance step changes. Conversely, although $I_{\rm o}$, $V_{\rm o}$, and $\theta_{\rm zvs}$ (solid and dotted lines in Fig. 9) in each set of experiments drop or rise rapidly, they gradually return to the set values with the help of the proposed nonlinear controller and traditional PI controller.

In addition, due to the traditional PI controller is designed based on the simplified linear model, the performance of the control loop is sensitive to the changes in load. Compared with the traditional PI controller, the nonlinear control adopted in this article enables the system to obtain a fixed response speed in 10 ms even if the load resistance of the IPT system changes.

B. Experimental Verification

An IPT hardware prototype is built for the wireless charging system as shown in Fig. 10, which consists of a dc voltage source, a full-bridge inverter, a symmetric S–S compensated resonant network, a rectifier and several switchable loads. The main parameters of the components are shown in Table I, where the value of the mutual inductance is measured at a power transfer distance of 20 cm. The ESRs of the primary and secondary side resonance networks are measured using an LCR meter (Agilent4263B). In addition, the diameters of the two coaxial coils are the same, whose rectangular outer ring is 90 cm × 70 cm. Each coil is built with four turns of Liz-wire, whose diameter is 6 mm and consisting of 2000 isolated strands.

Since the derived nonlinear control law is computationally complex, the controllers of the control loop are implemented with two MCUs, namely, an FPGA(XC6SLX9-3TQG144I) and an ARM (STM32F407VGT). This is because the mathematical library of STM32F407VGT can fully support the mathematical computation that required by the nonlinear control law. Once the MCUs complete the computation, the MOSFETs of the inverter are driven by the driving circuit to implement feedback control of the IPT system.

The objective of this article is to reduce the sensitivity of the system performance to the operating points. In this section, the authors compare the proposed nonlinear control scheme with a traditional PI controller using the experimental prototype. In addition, to imitate the changes of the operating point caused by the set value modification, the set values of the output current $I_{\rm o}$, output voltage $V_{\rm o}$ and ZVS angle $\theta_{\rm zvs}$ are defined as the following cases: 1) $V_{\rm o\_set}$ decreases from 100 to 50 V; 2) $V_{\rm o\_set}$ rises from 50 to 100 V; 3) $I_{\rm o\_set}$ decreases from 15 to 10 A; 4) $I_{\rm o\_set}$ rises from 10 to 15 A; 5) $\theta_{\rm zvs\_set}$ decreases from 20° to

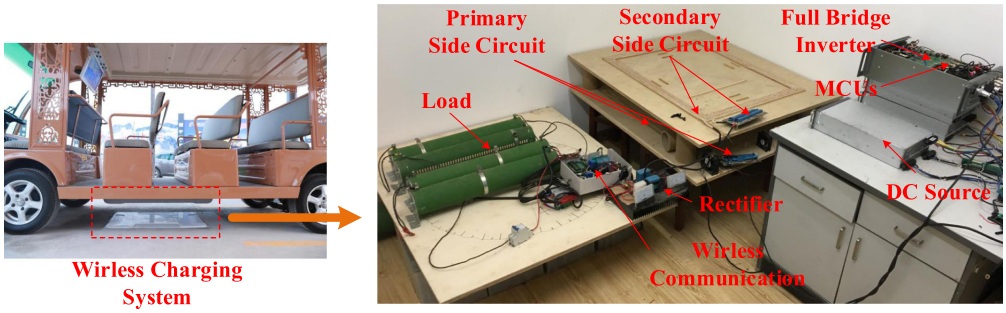

Fig. 10. Hardware prototype of the proposed wireless charging system.

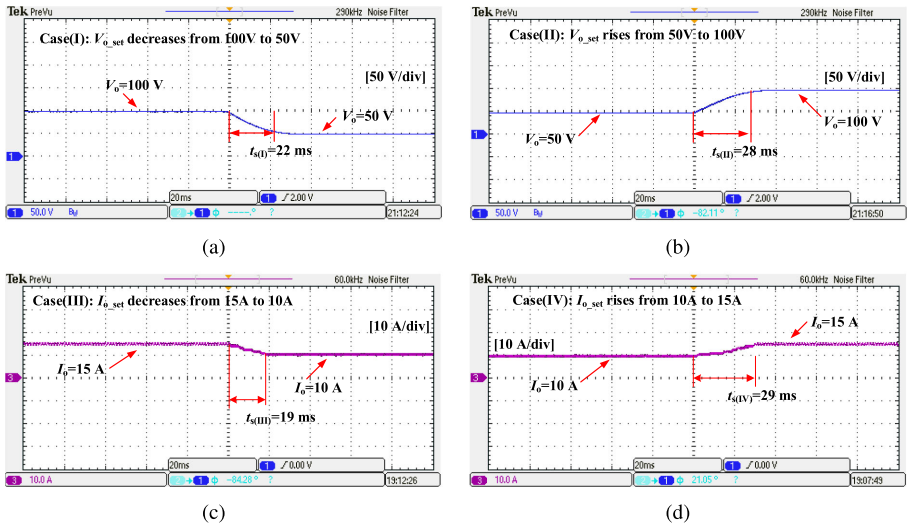

Fig. 11. Dynamic response curves of a traditional PI controller controlled IPT system with varying set values. (a) Response curve of $V_{\rm o}$ for $V_{\rm o\_set}$ decreases from 100 to 50 V. (b) Response curve of $V_{\rm o}$ for $V_{\rm o\_set}$ rises from 50 to 100 V. (c) Response curve of $I_{\rm o}$ for $I_{\rm o\_set}$ decreases from 15 to 10 A. (d) Response curve of $I_{\rm o}$ for $I_{\rm o\_set}$ rises from 10 to 15 A.

10°; and 6) $\theta_{\rm zvs\_set}$ rises from 10° to 20°. In the experiments, the step changes of the set values are triggered by an additional host computer through RS-485.

The dynamic response curves of $I_{\rm o}$ and $V_{\rm o}$ with a traditional PI controller at different cases are captured by an oscilloscope (Tektronix DPO 2004B) and shown in Fig. 11. In addition, Fig. 12 shows the dynamic response curves of $I_{\rm o}$ and $V_{\rm o}$ with the designed nonlinear controller.

Figs. 11 and 12 show that both $I_{\rm o}$ and $V_{\rm o}$ can realize tracking control when the set values change. However, it can be seen that the settling times of the traditional PI controller in Fig. 11 are sensitive to the modification of $V_{\rm o\_set}$ and $I_{\rm o\_set}$. In Fig. 11(a) and (c), when the set values $V_{\rm o\_set}$ and $I_{\rm o\_set}$ decrease from 100 V and 15 A to 50 V and 10 A, the outputs $V_{\rm o}$ and $I_{\rm o}$ need 22 ms and 19 ms, respectively, to catch up with the new set values. In Fig. 11(b) and (d), however, when the operating point of the system changes, that is, the set values $V_{\rm o\_set}$ and $I_{\rm o\_set}$ rise from 50 V and 10 A to 100 V and 15 A, respectively, it will take 28 ms and 29 ms for $V_{\rm o}$ and $I_{\rm o}$ to reach the set values.

Therefore, the fluctuation ratio of the settling times for both control loops with a traditional PI controller is 27.3% and 52.6%, respectively. The reason for this phenomenon is that the parameters of the traditional PI controller are all designed based on the simplified small signal linear model, which is obtained at a static operating point. When the set value $V_{\rm o\_set}$ or $I_{\rm o\_set}$ changes, the operating point of IPT system will deviate from the point where the parameters were designed. Therefore, the control performance of the controller is sensitive to the operating point.

Utilizing the proposed exact linearization algorithm, the dynamic nonlinear model of IPT system can be accurately transformed into a linear one. Therefore, with the proposed nonlinear controller, the IPT system in Fig. 12 can obtain a fixed dynamic performance even if the operating point changes. Referring to Fig. 12, one can see that the settling times of Fig. 12(a)–12(d) are 10, 11, 11, and 9 ms, respectively. Moreover, compared with the traditional PI controller, the fluctuation ratio of the settling times is optimized to 10% for the voltage loop and to 18.2% for the current loop.

The same tendency can also be observed in the ZVS angle control loop, as shown in Fig. 13. The dynamic waveforms of i_1 and $v_{\rm ab}$ for a traditional PI controller are plotted in Fig. 13(a)

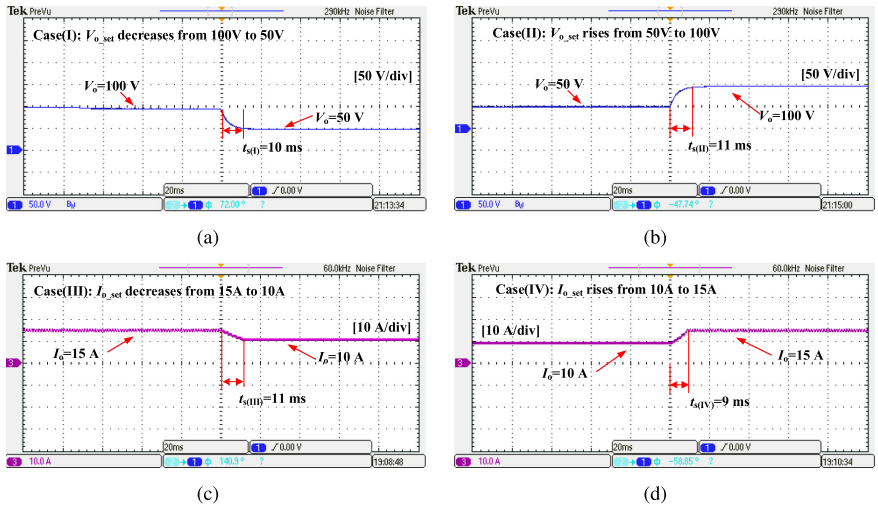

Fig. 12. Dynamic response curves of the proposed nonlinear controller controlled IPT system with varying set values. (a) Response curve of $V_{\rm o}$ for $V_{\rm o\_set}$ decreases from 100 to 50 V. (b) Response curve of $V_{\rm o}$ for $V_{\rm o\_set}$ rises from 50 to 100 V. (c) Response curve of $I_{\rm o}$ for $I_{\rm o\_set}$ decreases from 15 to 10 A. (d) Response curve of $I_{\rm o}$ for $I_{\rm o\_set}$ rises from 10 to 15 A.

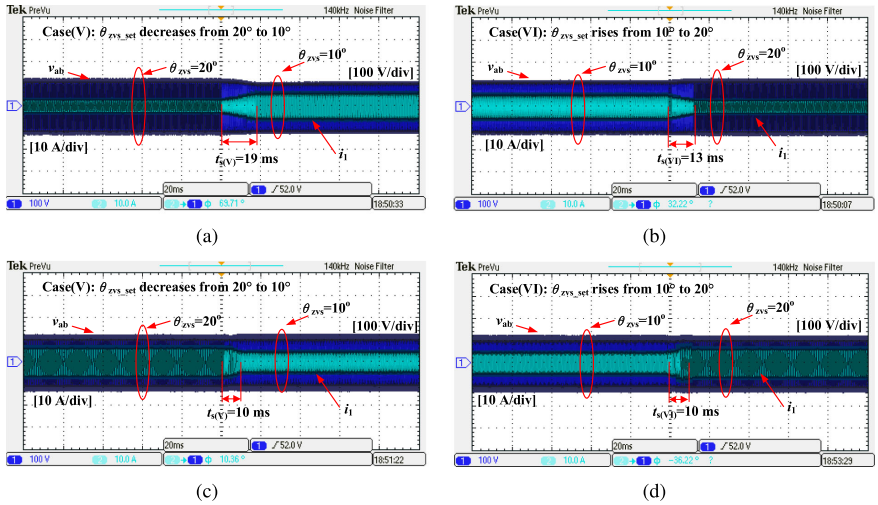

Fig. 13. Dynamic waveforms of i_1 and $v_{\rm ab}$ with varying set values. (a) Traditional PI controller for $\theta_{\rm zvs\_set}$ decreases from 20° to 10°. (b) Traditional PI controller for $\theta_{\rm zvs\_set}$ rises from 10° to 20°. (c) Proposed nonlinear controller for $\theta_{\rm zvs\_set}$ decreases from 20° to 10°. (d) Proposed nonlinear controller for $\theta_{\rm zvs\_set}$ rises from 10° to 20°.

and (b). Fig. 13(c) and (d) displays the dynamic waveforms of i_1 and $v_{\rm ab}$ under the action of the proposed nonlinear control scheme. Besides, the steady-state waveforms of i_1 and $v_{\rm ab}$, where $\theta_{\rm zvs\_set} = 10^{\rm o}$ and $\theta_{\rm zvs\_set} = 20^{\rm o}$ are plotted in Fig. 14(a) and (b).

One can see that the ZVS angle $\theta_{\rm zvs}$ needs 19 ms for $\theta_{\rm zvs\_set}$ decreasing from 20° to 10° and 13 ms for $\theta_{\rm zvs\_set}$ rising again to 20°, respectively, to reach the steady states, as shown in Fig. 13(a) and (b). Thus, the fluctuation ratio of the settling time for ZVS operating loop with traditional PI controller is 31.6%. However, with the help of the proposed nonlinear controller, the settling times in Fig. 13(c) and (d) are both 10 ms without any fluctuation. This proves that the nonlinear controller can make the ZVS angle control loop obtain a fixed response speed when the operating point changes.

According to (44)–(48), one obtains the theoretical and experimental transmission efficiency of the proposed IPT system, which are depicted in Fig. 15. We can see that the experimental transmission efficiency matches the theoretical curve. The maximum transmission efficiency of 93.9% is observed at the load resistance of 5 Ω. In addition, the transmission efficiency gradually decreases to the load raising. This implies that the transmission efficiency of the system can be optimized by the proposed controller.

C. Comparison to Previous Control Methods

In recent years, different control methods for achieving CC/CV charging or ZVS operating are reported. The control strategy, parameter design method, and dynamic performance

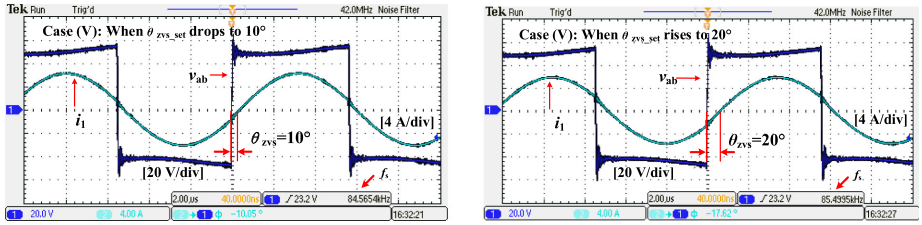

(a) (b)

Fig. 14. Steady-state waveforms of i_1 and $v_{\rm ab}$ when the set value of $\theta_{\rm zvs\_set}$ changes. (a) $\theta_{\rm zvs\_set}$ is 10°. (b) $\theta_{\rm zvs\_set}$ is 20°.

TABLE II
COMPARISON OF THIS ARTICLE WITH PREVIOUS CONTROL METHODS

Control Loop	Refference@year	Control Strategy	Parameter Design Method	Dynamic Performance	Sensitive to Operating Point
CC/CV Charging	[4]@2018	Decoupled Control	Zero-Pole Configuration	@CV mode<420 ms @CC mode< 435 ms	YES
	[1]@2019	Dual-Phase-Shift Control	Empirical	@CV mode<225 ms @CC mode< 440 ms	YES
	[22]@2020	Dual-Phase-Shift Control	Empirical	<650 ms	YES
	[16]@2018	Double Loop Control	Empirical	@CV mode<25 ms @CC mode< 30 ms	YES
	[9]@2019	H-Infinity Robust Control	Multiobjective Optimization	5.3-19 ms	Uncertain
	This paper	Nonlinear Control	Damping Coefficient	@CV/CV mode= 10 ms	NO
ZVS Operating	[4]@2018	Decoupled Control	Zero-Pole Configuration	<200 ms	YES
	[1]@2018	Accurate ZVS Angle Control	Empirical	<40 ms	YES
	[29]@2019	PI Control	Amplitude and Phase	<20 ms	YES
	[21]@2019	Phase-Shift Control	Empirical	<500 ms	YES
	This paper	Nonlinear Control	Damping Coefficient	@CV/CV mode= 10 ms	NO

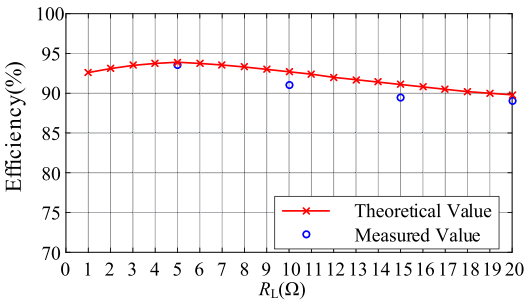

Fig. 15. Theoretical and experimental transmission efficiencies of the proposed IPT system versus load resistance.

of their experimental prototypes are summarized and listed in Table II. Due to different system parameters and circuit structures are used for each setup, a fair comparison among those control methods is difficult to obtain. Then, the emphasis of this article is focused on the dynamic response speed of the controllers at different operating points.

Observation of the dynamic reposed speeds indicates that as the system operating mode or load resistance changes, the settling times in previous studies will fluctuate. Compared with the advanced dynamic control above, the nonlinear control scheme adopted in this article makes the IPT system to obtain a fixed dynamic performance, which is consistent with the requirements. Furthermore, rather than the empirical method adopted by most control methods, the parameters of the proposed control method are optimized by designing the damping coefficient.

Although the usage of nonlinear control reduces the sensitivity of the system performance to the operating points, the dynamic performance of the controller can be further improved. In the future works, a load estimation method is expected to avoid the wireless communication link, thereby further improving the dynamic performance of the system.

VI. CONCLUSION

An exact linearization algorithm and nonlinear control method were proposed in this article to reduce the sensitivity of the system performance for CC/CV charging and ZVS operating control loops when the operating point changes. The process of the exact linearization algorithm consists of selecting vector fields, solving the intergralcurve, and deriving the coordinate mapping. By using the proposed algorithm, the dynamic nonlinear model of the IPT system can be linearized into a linear one at whole operation points. Moreover, based on the linear model and coordinate mapping, a nonlinear control law was obtained by designing a linear controller in the linear space and then mapping it to the nonlinear space. Simulation and hardware prototype were established in this article to realize CC/CV charging and ZVS operating. Compared with the traditional PI controller, the nonlinear control scheme adopted in this paper enables the IPT system to obtain a fixed dynamic performance even if the operating point changes.

REFERENCES

[1] Y. Jiang, L. Wang, Y. Wang, J. Liu, X. Li, and G. Ning, "Analysis, design and implementation of accurate ZVS angle control for EV's battery charging in wireless high power transfer," *IEEE Trans. Ind. Electron.*, vol. 66, no. 5, pp. 4075–4085, May 2019.

[2] B. Vu, D. H. Tran, and W. Choi, "Implementation of the constant current and constant voltage charge of inductive power transfer systems with the double-sided lcc compensation topology for electric vehicle battery charge applications," *IEEE Trans. Power Electron.*, vol. 33, no. 9, pp. 7398–7410, Sep. 2018.

[3] J. Shin *et al.*, "Design and implementation of shaped magnetic-resonance-based wireless power transfer system for roadway-powered moving electric vehicles," *IEEE Trans. Ind. Electron.*, vol. 61, no. 3, pp. 1179–1192, Mar. 2014.

[4] C. Chen *et al.*, "Modeling and decoupled control of inductive power transfer to implement constant current/voltage charging and ZVS operating for electric vehicles," *IEEE Access*, vol. 6, pp. 59 917–59 928, 2018.

[5] Z. H. Wang, Y. P. Li, Y. Sun, C. S. Tang, and X. Lv, "Load detection model of voltage-fed inductive power transfer system," *IEEE Trans. Power Electron.*, vol. 28, no. 11, pp. 5233–5243, Nov. 2013.

[6] Q. Chen, S. C. Wong, K. T. Chi, and X. Ruan, "Analysis, design, and control of a transcutaneous power regulator for artificial hearts," *IEEE Trans. Biomed. Circuits Syst.*, vol. 3, no. 1, pp. 23–31, Feb. 2009.

[7] L. Xun and S. Y. Hui, "Simulation study and experimental verification of a universal contactless battery charging platform with localized charging features," *IEEE Trans. Power Electron.*, vol. 22, no. 6, pp. 2202–2210, Nov. 2007.

[8] J. Zhou, B. Zhang, W. Xiao, D. Qiu, and Y. Chen, "Nonlinear parity-time-symmetric model for constant efficiency wireless power transfer: Application to a drone-in-flight wireless charging platform," *IEEE Trans. Ind. Electron.*, vol. 66, no. 5, pp. 4097–4107, May 2019.

[9] M. Yang, Y. Li, H. Du, C. Li, and Z. He, "Hierarchical multiobjective h-infinity robust control design for wireless power transfer system using genetic algorithm," *IEEE Trans. Control Syst. Technol.*, vol. 27, no. 4, pp. 1753–1761, Jul. 2019.

[10] K. Song, Z. Li, J. Jiang, and C. Zhu, "Constant current/voltage charging operation for series-series and series-parallel compensated wireless power transfer systems employing primary-side controller," *IEEE Trans. Power Electron.*, vol. 33, no. 9, pp. 8065–8080, Sep. 2018.

[11] J. Tian and A. P. Hu, "A dc-voltage-controlled variable capacitor for stabilizing the ZVS frequency of a resonant converter for wireless power transfer," *IEEE Trans. Power Electron.*, vol. 32, no. 3, pp. 2312–2318, Mar. 2017.

[12] P. Tan, H. He, and X. Gao, "A frequency-tracking method based on a SOGI-PLL for wireless power transfer systems to assure operation in the resonant state," *J. Power Eletron.*, vol. 16, no. 3, pp. 1056–1066, 2016.

[13] D. Gunji, T. Imura, and H. Fujimoto, "Stability analysis of constant power load and load voltage control method for wireless in-wheel motor," in *Proc. Int. Conf. Power Electron.*, June 2015, pp. 1944–1949.

[14] X. Qu, H. Han, S. Wong, T. Chi, and W. Chen, "Hybrid IPT topologies with constant current or constant voltage output for battery charging applications," *IEEE Trans. Power Electron.*, vol. 30, no. 11, pp. 6329–6337, Nov. 2015.

[15] B. Wang, A. P. Hu, and D. Budgett, "Maintaining middle zero voltage switching operation of parallel-parallel tuned wireless power transfer system under bifurcation," *IET Power Electron.*, vol. 7, no. 7, pp. 78–84, 2014.

[16] Y. Li, J. Hu, F. Chen, Z. Li, Z. He, and R. Mai, "Dual-phase-shift control scheme with current-stress and efficiency optimization for wireless power transfer systems," *IEEE Trans. Circuits Syst. I Regular Papers*, vol. 65, no. 9, pp. 3110–3121, Sep. 2018.

[17] X. Yuan, Y. Xiang, W. Yan, and X. Yan, "Neural networks based PID control of bidirectional inductive power transfer system," *Neural Process. Lett.*, vol. 43, no. 3, pp. 837–847, 2015.

[18] Q. Zhang, Y. Huang, T. Niu, and X. Chenyang, "Analysis and control of dynamic wireless charging output power for electric vehicle," in *Proc. Int. Conf. Intell. Comput. Technol. Autom.*, Oct 2017, pp. 349–354.

[19] A. K. Swain, M. J. Neath, U. K. Madawala, and D. J. Thrimawithana, "A dynamic multivariable state-space model for bidirectional inductive power transfer systems," *IEEE Trans. Power Electron.*, vol. 27, no. 11, pp. 4772–4780, Nov. 2012.

[20] A. K. Swain, S. Devarakonda, and U. K. Madawala, "Modeling, sensitivity analysis, and controller synthesis of multipickup bidirectional inductive power transfer systems," *IEEE Trans. Ind. Informat.*, vol. 10, no. 2, pp. 1372–1380, May 2014.

[21] M. Kim, D.-M. Joo, and B. K. Lee, "Design and control of inductive power transfer system for electric vehicles considering wide variation of output voltage and coupling coefficient," *IEEE Trans. Power Electron.*, vol. 34, no. 2, pp. 1197–1208, Feb. 2019.

[22] Z. Huang, S.-C. Wong, and C. K. Tse, "Comparison of basic inductive power transfer systems with linear control achieving optimized efficiency," *IEEE Trans. Power Electron.*, vol. 35, no. 3, pp. 3276–3286, Mar. 2020.

[23] D. M. Beams and A. Papasani, "State-variable analysis of wireless power transfer networks for linear and nonlinear loads," in *Proc. IEEE Int. Midwest Symp. Circuits Syst.*, Aug. 2013, pp. 505–508.

[24] E. Bou-Balust, A. E. Aroudi, P. Fisher, and E. Alarcon, "Unveiling nonlinear dynamics in resonant inductively coupled wireless power transfer," in *Proc. IEEE Int. Symp. Circuits Syst.*, 2014, pp. 2612–2615.

[25] A. Kurs, A. Karalis, R. Moffatt, J. D. Joannopoulos, P. Fisher, and M. Soljai, "Wireless power transfer via strongly coupled magnetic resonances," *Science*, vol. 317, no. 5834, pp. 83–86, 2007.

[26] H. Li, J. Li, L. Huang, K. Wang, and X. Yang, "A novel dynamic modeling method for wireless power transfer systems," in *Proc. Appl. Power Electron. Conf. Expos.*, 2015, pp. 2740–2743.

[27] H. Li, K. Wang, L. Huang, W. Chen, and X. Yang, "Dynamic modeling based on coupled modes for wireless power transfer systems," *IEEE Trans. Power Electron.*, vol. 30, no. 11, pp. 6245–6253, Nov. 2015.

[28] Q. Deng *et al.*, "Modeling and control of inductive power transfer system supplied by multiphase phase-controlled inverter," *IEEE Trans. Power Electron.*, vol. 34, no. 9, pp. 9303–9315, Sep. 2019.

[29] J. Liu, Q. Deng, W. Wang, and Z. Li, "Modeling and control of inverter zero-voltage-switching for inductive power transfer system," *IEEE Access*, vol. 7, pp. 139 885–139 894, 2019.

[30] M. Kazimierczuk and D. Czarkowski, *Resonant Power Converters*. New York, NY, USA: Wiley, 2011, pp. 28–241.

[31] W. Zhang and C. C. Mi, "Compensation topologies of high-power wireless power transfer systems," *IEEE Trans. Veh. Technol.*, vol. 65, no. 6, pp. 4768–4778, Jun. 2016.

[32] J.-J. E. Slotine and W. Li, *Applied Nonlinear Control.* Englewood Cliffs, NJ, USA: Prentice Hall, 1991, pp. 170–175.

[33] F. P. Miller, A. F. Vandome, and J. McBrewster, *Integral Curve.* San Carlos, CA, USA: Alphascript, 2010, pp. 1–96.

[34] S. Varikkottil and F. D. J.L.,"Compact pulse position control-base inverter for high efficiency inductive power transfer to electric vehicle," *IET Power Electron.*, vol. 13, no. 1, pp. 86–95, 2020.

[35] Q. Deng, J. Liu, D. Czarkowski, M. Bojarski, E. Asa, and F. D. Leon, "Design of a wireless charging system with a phase-controlled inverter under varying parameters," *IET Power Electron.*, vol. 9, no. 13, pp. 2461–2470, 2016.

Chen Cheng received the B.S. degree in mechanical engineering from the Wuhan Institute of Bioengineering, Wuhan, China, in 2012, and the M.S. degree in control engineering and the Ph.D. degree in mechatronic engineering from Wuhan University, Wuhan, China, in 2015 and 2019, respectively.

In October 2019, he joined the School of Electrical Engineering, Naval University of Engineering, where he is currently a Lecturer. His research interests include wireless power transfer, system modeling, nonlinear control, and power system fault diagnosis.

Ye Zhihao received the B.S., M.Sc., and Ph.D. degrees in electrical engineering from the Naval University of Engineering, Wuhan, China, in 1997, 2000, and 2005, respectively.

In February 2005, he joined the School of Electrical Engineering, Naval University of Engineering, where he was a Lecturer from 2005 to 2006, and is currently a Professor with the School of Electrical Engineering. He was a Professor with the Naval Engineering Power Electronics Technology Institute, in 2012. His research interests include power system analysis, wireless power transfer, integrated power system and power system fault diagnosis.

Huang Jing received the B.S. degree in electric power system and automation and the Ph.D. degree in electrical engineering from the Naval University of Engineering, Wuhan, China, in 2003 and 2010, respectively.

He is currently a Lecturer with the School of Electrical Engineering, Naval University of Engineering. His research interests include power system and automation.

Yu Yanjuan received the B.S. degree in control theory and applications and the Ph.D. degree in electrical engineering from Wuhan University, Wuhan, China, in 2013 and 2019, respectively.

In October 2019, she joined the School of Electrical Engineering, Naval University of Engineering, where she is currently a Lecturer. Her research interests include wireless power transfer, mathematical optimization and renewable energy accommodation.

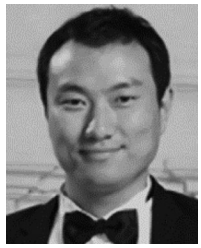

Xia Yihui was born in Henan, China, in 1987. He received the B.S., M.S., and Ph.D. degrees in electrical engineering from the School of Electrical Engineering, Naval University of Engineering, Wuhan, China in 2005, 2011, and 2015, respectively.

He is currently a Lecturer with the School of Electrical Engineering, Navy University of Engineering. His research interests include power electronics, electric machine drives, active power filters and matrix converters.

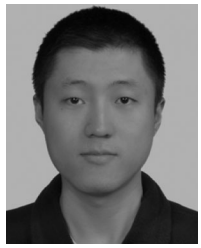

Gao Jianxin received M.S. and Ph.D. degrees in electrical engineering from the Naval University of Engineering, Wuhan, China, in 2011 and 2017, respectively.

He is currently a Lecturer with the School of Electrical Engineering, Naval University of Engineering, Wuhan, China. His research interests include electric machine design, numerical and analytical methods in electromagnetic, linear electric motors.

Zhou Hong received the B.S. degree from the Central South University of Technology (now the Central South University), Changsha, China, in 1982, the M.Sc. degree from Chongqing University, Chongqing, China, in 1988, and the Ph.D. degree from Wuhan University, Wuhan, China, in 2006.

He was an Assistant Engineer with Changshou Power Plant, Chongqing, from 1982 to 1985. He has been with the Wuhan University of Hydraulic and Electrical Engineering (now a part of Wuhan University), Wuhan, since 1992. He was the Head of the Department of Automation, Wuhan University, from 2002 to 2006, and has been a Professor with the Department since 2000. His main research interests include wireless power transfer, smart grid, and networked control systems.